The Astrophysical Journal, 925:28 (8pp), 2022 January 20 https://doi.org/10.3847/1538-4357/ac3916

The Birth Mass Function of Population III Stars

Muhammad A. Latif[1], Daniel Whalen[2], and Sadegh Khochfar[3]
[1] Physics Department, College of Science, United Arab Emirates University, PO Box 15551, Al-Ain, UAE; latifne@gmail.com
[2] Institute of Cosmology and Gravitation, University of Portsmouth, Portsmouth, PO1 3FX, UK
[3] Institute for Astronomy, University of Edinburgh, Royal Observatory, Blackford Hill, Edinburgh, EH9 3HJ, UK
Received 2021 March 4; revised 2021 October 30; accepted 2021 November 10; published 2022 January 21

Abstract

Population III stars ended the cosmic dark ages and began early cosmological reionization and chemical enrichment. However, in spite of their importance to the evolution of the early universe, their properties remain uncertain because of the limitations on previous numerical simulations and the lack of any observational constraints. Here, we investigate Population III star formation in five primordial halos using 3D radiation-hydrodynamical cosmological simulations. We find that multiple stars form in each minihalo and that their numbers increase over time, with up to 23 stars forming in one of the halos. Radiative feedback from the stars generates strong outflows, deforms the surrounding protostellar disk, and delays star formation for a few thousand years. Star formation rates vary with halo, and depend on the mass accretion onto the disk, the halo spin number, and the fraction of massive stars in the halo. The stellar masses in our models range from 0.1–37 $M_{\odot}$, and of the 55 stars that form in our models, 12 are $>10\,M_{\odot}$ and most of the others are 1–10 $M_{\odot}$. Our simulations thus suggest that Population III stars have characteristic masses of 1–10 $M_{\odot}$ and top-heavy initial mass functions with $\mathrm{dN/dM} \propto M_{*}^{-1.18}$. Up to 70% of the stars are ejected from their disks by three-body interactions that, along with ionizing UV feedback, limit their final masses.

Unified Astronomy Thesaurus concepts: Population III stars (1285)

1. Introduction

The emergence of Population III stars, 100–200 million yr after the Big Bang, ended the cosmic dark ages and began cosmic reionization, early chemical enrichment, and the formation of the first stellar black holes. Population III stars are expected to form in 10^5–10^6 $M_{\odot}$ primordial minihalos at $z = 20$–30, as a result of gravitational collapse induced by H_2 rovibrational line cooling in the absence of metals. Their initial mass function (IMF) is still an open question, and is central to our understanding of the high-redshift universe.

The first studies suggested that Population III stars have typical masses of a few hundred solar masses and form in isolation, one per halo (Abel et al. 2002; Bromm et al. 2002; Yoshida et al. 2008). However, recent numerical simulations have shown that the accretion disk at the center of the halo fragments into multiple clumps that can produce multiple stars (Clark et al. 2011; Latif et al. 2013; Hirano et al. 2014; Sharda et al. 2020). Greif et al. (2012) found that almost two thirds of such fragments later merge and that only a third had survived 10 yr after the formation of the protostar. Hirano et al. (2015) considered only one single star forming per minihalo, and found that their masses range from 10–1000 $M_{\odot}$. Stacy et al. (2016) performed a cosmological simulation with feedback from the most massive protostar only, and found that 37 sink particles form in one minihalo, with the most massive star growing to 20 $M_{\odot}$ in the first 5 kyr. The radiation-hydrodynamical simulations by Hosokawa et al. (2016), in which only one star was allowed to form in the disk, found that the star grows to 600 $M_{\odot}$ by clump migration (see also Latif & Schleicher 2015). However, it is not clear how radiation from multiple stars in the disk would affect the outcome of these studies.

Susa (2019) followed the collapse of a Bonner–Ebert sphere with a simple barotropic equation of state, without stellar feedback or chemistry, and found that the number of fragments in the disk increases with time after the onset of star formation ($\propto t^{0.3}$). More recently, Sugimura et al. (2020) simulated the collapse of a cloud extracted from a cosmological simulation at densities of $10^6\,\mathrm{cm}^{-3}$ with six-species chemistry and radiative feedback from protostars, and found that it formed a massive, wide binary system (60 and 70 $M_{\odot}$). These studies either included feedback from just one protostar in a cosmological environment, or they relied on idealized initial conditions to study the fragmentation in primordial gas clouds. No cosmological simulation of Population III star formation has ever included ionizing and dissociative feedback from all of the protostars in the cloud.

We have performed 3D radiation-hydrodynamical cosmological simulations of Population III star formation in five primordial halos at $z = 20$–30, with sink particles that mimic Population III stars and mass-dependent photodissociative and ionizing feedback from the protostars. The simulations are evolved for up to ∼20 kyr after the formation of the first star. We summarize our simulation setup and recipe for star formation and feedback in Section 2. Our main results are presented in Section 3, and we conclude in Section 4.

2. Numerical Method

We use the Enzo adaptive mesh refinement code (Bryan et al. 2014) for the simulations in our study. They are initialized at $z = 150$ with Gaussian primordial density fluctuations generated by MUSIC (Hahn & Abel 2011) and cosmological parameters from the Planck 2016 data release (Planck Collaboration et al. 2016). The simulation box is 300 h^{-1} ckpc on its side, with a top grid resolution of 256^3, and two additional static nested grids

centered on the halo, for an effective initial resolution of 1024^3. We allow up to 20 levels of refinement in the subvolume covering 20% of the top grid, which produce an effective spatial resolution of ∼10 au. Dark matter (DM) particles are split into 13 child particles, yielding an effective DM resolution of about 0.2 $M_\odot$. The Jeans length throughout the simulation is resolved by at least 32 cells. For further details about our refinement criteria, see Latif et al. (2021).

2.1. Sink Formation/Stellar Feedback

We use sink particles to represent Population III stars. Sinks are created in grid cells that meet the following conditions (Regan & Downes 2018; Latif et al. 2021): (1) it is at the maximum refinement level; (2) it is at the local minimum of the gravitational potential; (3) it has a convergent flow; (4) the gas density is higher than the Jeans density; and (5) the cooling time is shorter than the freefall time. These criteria typically create sinks at densities $\geqslant 10^{-12}$ gcm^{-3}. A sink particle can accrete gas from a radius of four cells, and any other particles forming within the accretion radius are immediately merged with the most massive one. Sink particles are also merged with the more massive sink if they come within each other's accretion radius. The velocity of the sink after accretion or a merger is determined from the conservation of momentum (Krumholz et al. 2004). The accretion rate of the sink is calculated from the mass influx at the accretion radius. Federrath et al. (2010) include the boundedness of the gas and the Jeans instability in their criteria, but Regan & Downes (2018) found that their effects on sink formation are less important than those of the criteria listed above.

Radiative feedback from a protostar depends on its effective temperature and luminosity, which can be determined from its accretion history, mass, and radius. Population III protostars are usually born on the Hayashi track, with effective temperatures of ∼5000 K, and later transition to the Henyey track, before eventually reaching the main sequence (see Section 2 of Stacy et al. 2016, and references therein, hereafter S16). The radius of the protostar depends on whether accretion proceeds through a thin disk or is spherical (Hosokawa et al. 2010). In either case, the star begins Kelvin–Helmholtz contraction at

$$M_* \sim 7\left(\frac{\dot{M}}{10^{-3}\,M_\odot/yr}\right)^{0.27} M_\odot, \quad (1)$$

where $\dot{M}$ is the accretion rate of the protostar (Omukai & Palla 2003; Hosokawa et al. 2010; Smith et al. 2012). S16 found that the star only produces ionizing UV after growing to $\gtrsim 10\ M_\odot$. We assume here that protostars remain cool and do not produce any ionizing radiation until they reach 10 $M_\odot$, when they begin to emit both IR and ionizing UV. The exact transition to the zero-age main sequence is uncertain, and depends on the geometry of the accretion (i.e., whether disk or spherical) and the accretion rates of the protostars. S16 compared several models for this transition, and found that they only begin to converge at $>5\,M_\odot$. Furthermore, disk accretion models exhibit an abrupt increase in stellar luminosity above a few solar masses (see the right panel of Figure 1 in Stacy et al. 2016). Our choice of switching on ionizing UV at 10 $M_\odot$ is thus consistent with previous studies (Omukai & Palla 2003; Hosokawa et al. 2010; Smith et al. 2012; Stacy et al. 2016).

We therefore set $T_{\rm eff} = 5000$ K when $M_* \leqslant 10\ M_\odot$ (Hosokawa et al. 2013) and $T_{\rm eff} = 10^{4.759}$ when $M_* > 10\ M_\odot$ (Schaerer 2002), and assume that the protostellar mass is equal to the sink mass. Hosokawa et al. (2016) found that short bursts of rapid accretion can lead to protostellar expansion even above 10 $M_\odot$. To account for such episodes, we assume that $T_{\rm eff} = 5000$ K above a threshold accretion rate of $\sim 10^{-2}\ M_\odot$ yr^{-1}, and $T_{\rm eff} = 10^{4.759}$ below this rate. Stars above 10 $M_\odot$ are approximated as blackbodies with $T_{\rm eff} = 10^{4.759}$. The luminosity of a star scales with mass, but $T_{\rm eff}$ is held constant for simplicity, because it does not change much over the masses of the stars in our study (see Table 3 of Schaerer 2002). This approximation has little effect on the dynamics of the ionization fronts (I-fronts) of the stars because ionized gas temperatures do not vary strongly with photon energy, hence $T_{\rm eff}$ (Whalen & Norman 2008).

We use the MORAY ray-tracing radiation transport module (Wise & Abel 2011) to propagate radiation from the stars and partition the flux into four energy bins: one for the photodetachment of H^- (2.0 eV), one for the Lyman–Werner (LW) photodissociation of H_2 and H_2^+ (12.8 eV), and two for the ionizations of H and He (14.0 and 25.0 eV, respectively). Energy fractions of 0.3261, 0.1073, 0.3686, and 0.1965 are used in bins 1-4, respectively, and are taken from Table 4 of Schaerer (2002). Stars below 10 $M_\odot$ are assumed only to be sources of IR peaking at 2 eV. Radiation pressure due to momentum transfer by ionizations is included in MORAY (Wise et al. 2012).

2.2. Primordial Gas Chemistry

We use the nonequilibrium primordial gas reaction network from Turk et al. (2012), which is based on Abel et al. (1997) and Anninos et al. (1997), to evolve the H, H^+, H^-, He, He^+, He^{2+}, H_2, H_2^+, and e^- mass fractions. Collisional ionization and excitation cooling by H and He, recombination cooling, H_2 cooling, inverse Compton cooling, bremsstrahlung cooling, collisionally-induced emission cooling at high densities, and heating due to three-body reactions are all included in the updates to the gas energy equation. At densities above 10^{-14} g cm^{-3}, the gas becomes optically-thick to H_2 lines, so we reduce the optically-thin H_2 cooling rate by fitting factors from Ripamonti & Abel (2004). We use the Glover & Abel (2008) rate coefficients for three-body H_2 formation and the Wolcott-Green et al. (2011) model for H_2 self-shielding from LW radiation. We do not include deuterium or related species, because HD cooling mostly occurs in relic H II regions or shock-heated gas during major mergers, which can boost D^+ abundances (Greif et al. 2008; McGreer & Bryan 2008; Bovino et al. 2014). Our chemistry solver is self-consistently coupled to hydrodynamics and radiation transport.

3. Results

We simulated Population III star formation in five halos whose masses and collapse redshifts are listed in Table 1. They are evolved from different Gaussian random fields and have spin parameters that are sampled from the peaks in the spin distributions of minihalos from large-scale numerical simulations (Bullock et al. 2001). The 20 levels of refinement allow us to follow the collapse of gas in these halos, from kpc scales down to about 10 au. The trace amounts of H_2 formed in the gas phase reactions are boosted during virialization and trigger

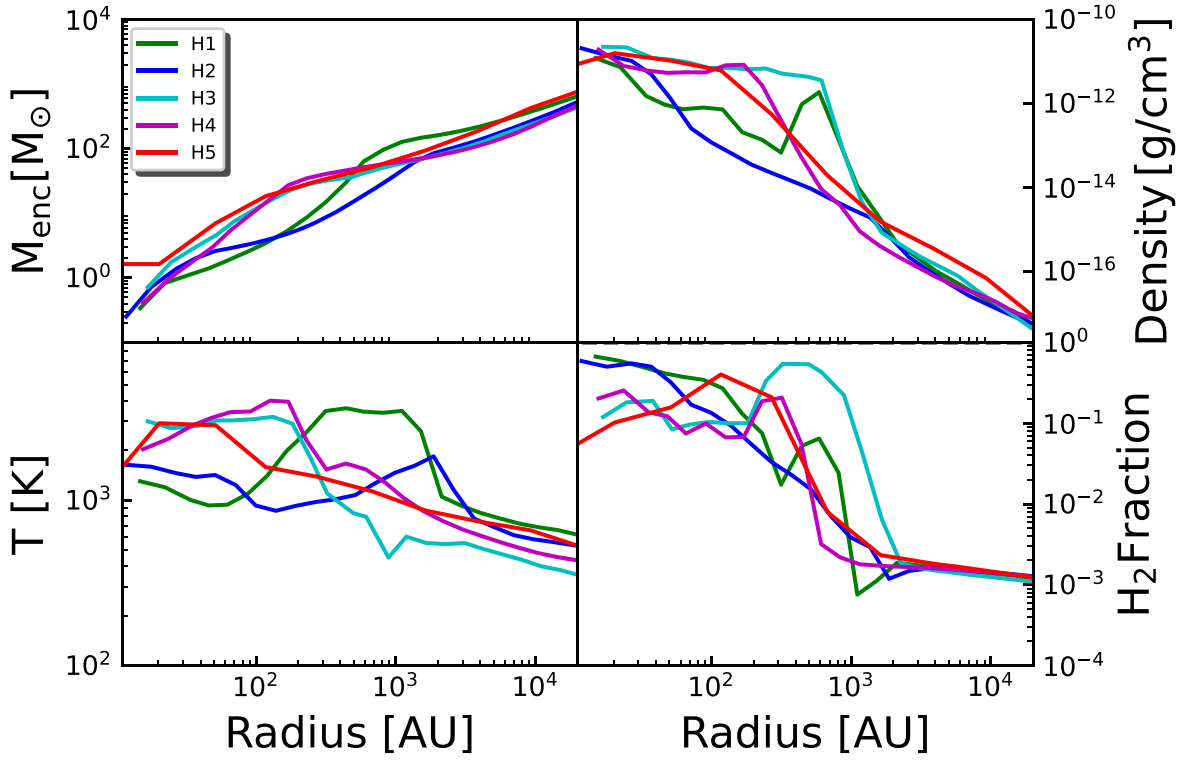

Figure 1. Spherically averaged radial profiles of gas density, temperature, H_2 mass fraction, and enclosed mass at the onset of star formation in the five halos.

Table 1
Virial Masses, Collapse Redshifts, Spin Parameters λ, and Total Masses of the Population III Stars of the Halos in Our Study

Halo	z	Mass ($M_\odot$)	λ	Stellar Mass ($M_\odot$)
1	22	2.7×10^5	0.042	166.02
2	28	1.8×10^5	0.011	83.64
3	20	3.2×10^5	0.016	31.57
4	21	2.7×10^5	0.025	27.10
5	22	5.2×10^5	0.025	56.59

collapse in halos above a few 10^5 $M_\odot$. Collapse leads to the formation of an accretion disk in each halo, with an initial mass of $\sim$100 $M_\odot$ and radius of a few hundred au. In Figure 1, we show spherically averaged profiles of density, temperature, H_2 mass fraction, and enclosed mass in the center of each halo at the onset of star formation in the disks.

The densities rise from $\sim 10^{-17}$ g cm^{-3} to 10^{-11} g cm^{-3} from 20,000 au down to 10 au. Above 10^{-16} g cm^{-3}, three-body reactions boost H_2 mass fractions from $\sim 10^{-3}$ to as high as 0.5 at the center of the disks. H_2 initially cools gas to a few hundred K, but at the high densities closer to the center of the disks the gas becomes opaque to H_2 lines that, together with heating due to the three-body formation of H_2, raises the temperatures to a few thousand K. The H_2 fractions in the disks vary from 0.2–0.4 at their centers, to a few 10^{-1} at their outer edges.

The small differences in temperatures and H_2 abundances between the disks are due to the variations in density between the halos. As shown in Figure 2, the accretion rates onto the disks fluctuate between 10^{-4} $M_\odot$ yr^{-1} and 0.05 $M_\odot$ yr^{-1}, but average $\sim$0.01 $M_\odot$ yr^{-1}, except in halo 2, which has about half this rate. These rates are a factor of a few lower than the estimates from $M_{\rm Jeans}/T_{ff} \propto T^{3/2}$, which suggests that accretion is regulated by radiation from the stars.

Density and temperature images of the halos are shown in Figures 3 and 4. The mass of the first star to form in halo 1 is 20 $M_\odot$, and its radiation dissociates H_2 and ionizes and heats the gas to $\sim 10^4$ K, which generates a strong shock that drives the gas outward (see Figure 3). The outflows have densities of 10^{-15}–10^{-13} g cm^{-3}. About 920 yr later, a second, 11 $M_\odot$ star forms in the disk. Radiation pressure from the stellar flux compresses the disk, and leads to the formation of 4 more stars over the next few hundred yr. The radiation from these stars breaks up the disk and creates dense clumps in which new stars form, and the number of stars rises to 10 over the next 4 kyr. Subsequently, two short starbursts at 6 kyr and 8 kyr increase the number of stars to 16 and 21, respectively. Stars continue to form in dense clumps over time, and generate strong outflows, but they are unable to halt star formation because of the infall from larger scales at rates of a few 10^{-3} $M_\odot$ yr^{-1}. The mass inflow rates onto the disk are quite intermittent, and are mainly regulated by the radiation from stars.

The first star in halo 2 is 25 $M_\odot$, and its ionizing UV flux launches a strong outflow that suppresses star formation in the disk for about 3.6 kyr. The second star is 16 $M_\odot$, and its radiation distorts the disk and forms an annular structure. The UV ionizing feedback from both of the stars continues to quench star formation for the next 6 kyr, and then 6 more stars form over the next 4.6 kyr, with masses of 25, 7, 7, 1.0, 0.5, and 0.8 $M_\odot$, respectively. The radiation from these stars deforms the disk, suppresses star formation, and creates an annular shell of gas. In the final 8 kyr, only one subsolar-mass object (0.001 $M_\odot$) forms, which may evolve into a Population III brown dwarf. Star formation drives a series of outflows that collide with the infalling gas and are eventually absorbed by the surrounding dense medium at radii less than 3000 au.

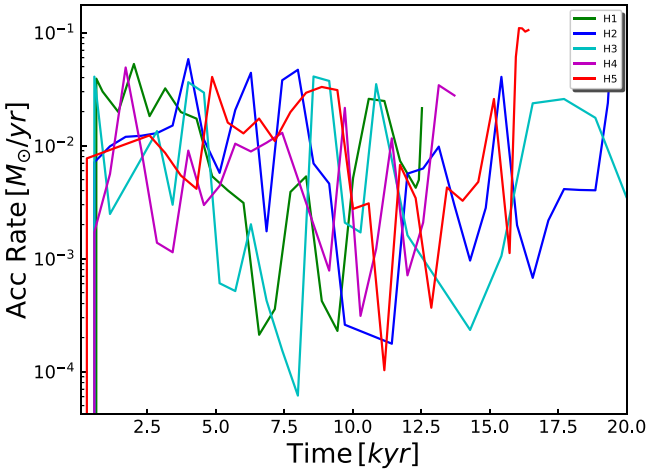

Figure 2. Accretion rates for the disks (central 300 au) in each halo.

Most sink masses are subsolar or a few $M_\odot$, but a few that are born in dense clumps are massive at birth. The mass of the first star in halo 3 is 2 $M_\odot$, and a second, 2 $M_\odot$ star forms after 790 yr. The disk in this halo is quite compact, and rotates at higher rates than the disks in halos 1 and 2, with initial mass accretion rates that are a factor of a few lower than those in the other halos. 4 stars form in halo 3 in the first 5 kyr, compared to the 2 stars that form in this time in halo 2, but they have low masses ($<5\,M_\odot$). In total, 10 stars form over 12 kyr. One is 13 $M_\odot$ and the others are 0.1–10 $M_\odot$. The star formation rates in halo 3 are similar to those in halo 2, but the stars are less massive.

A 3 $M_\odot$ star forms first in halo 4, and then six more stars appear over the next 2 kyr. All are low-mass stars ($<5\,M_\odot$), except one that is $\sim$18 $M_\odot$, and two of the stars later merge. Ionizing UV from the most massive star drives flows that sweep up gas into an expanding, ring-like structure. The ring

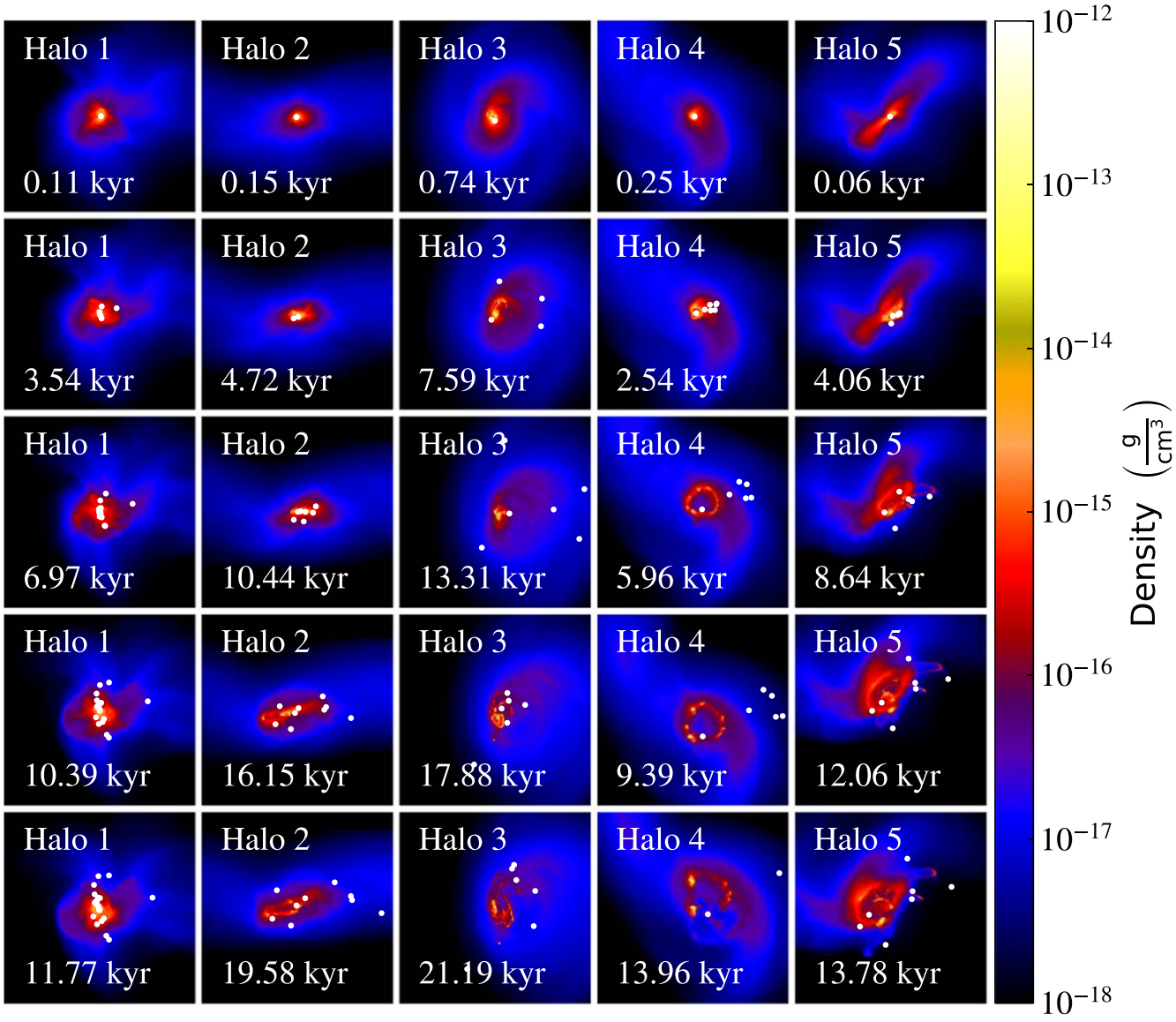

Figure 3. Density projections of the central 0.2 pc of each halo. Each column shows the time evolution of the halo, from top to bottom, and the times are measured from the formation of the first star in the halo. The white dots mark the locations of star particles.

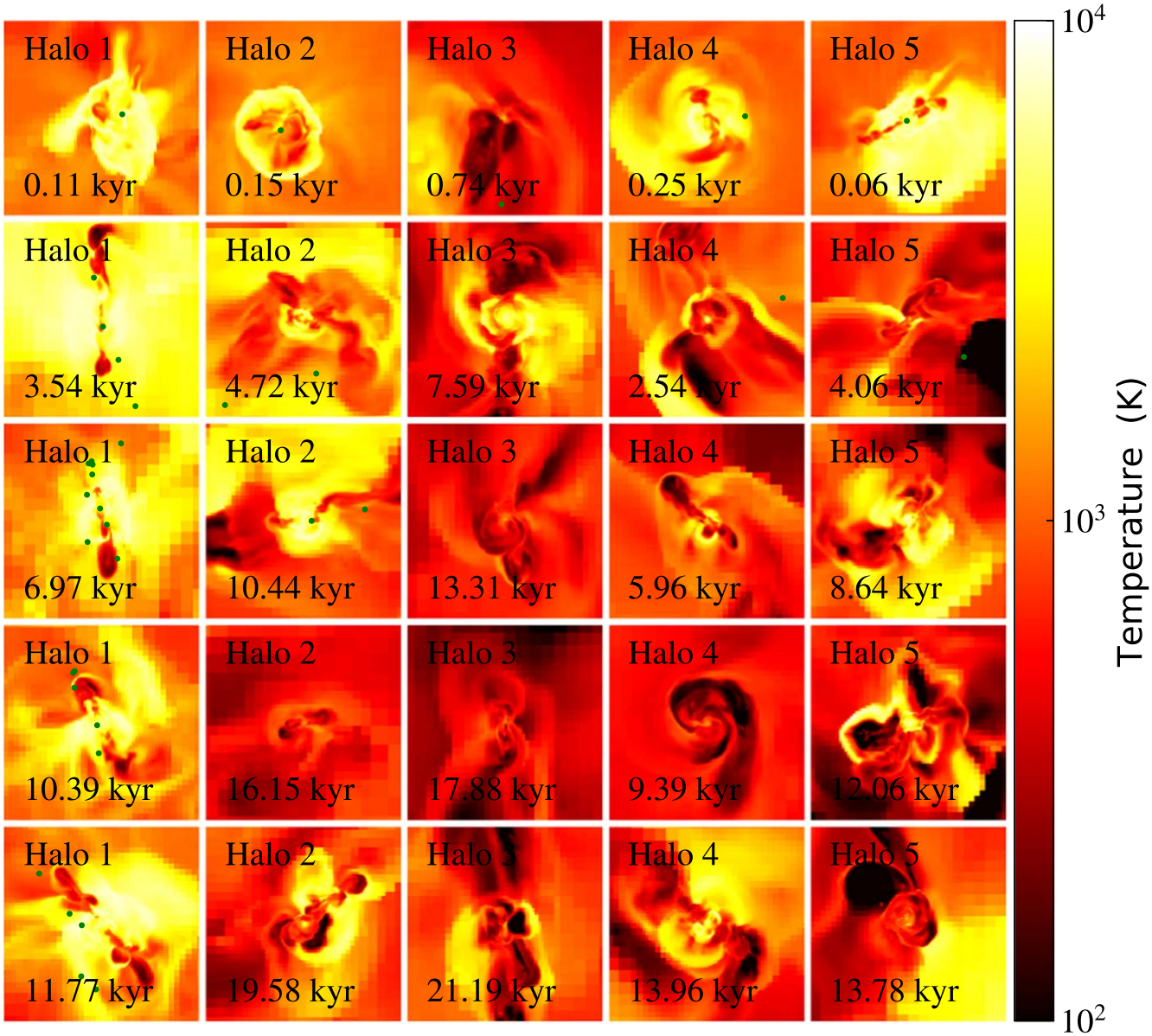

Figure 4. Temperature slices along the *x*-direction in the central 2000 au of each halo. The green dots mark the positions of star particles.

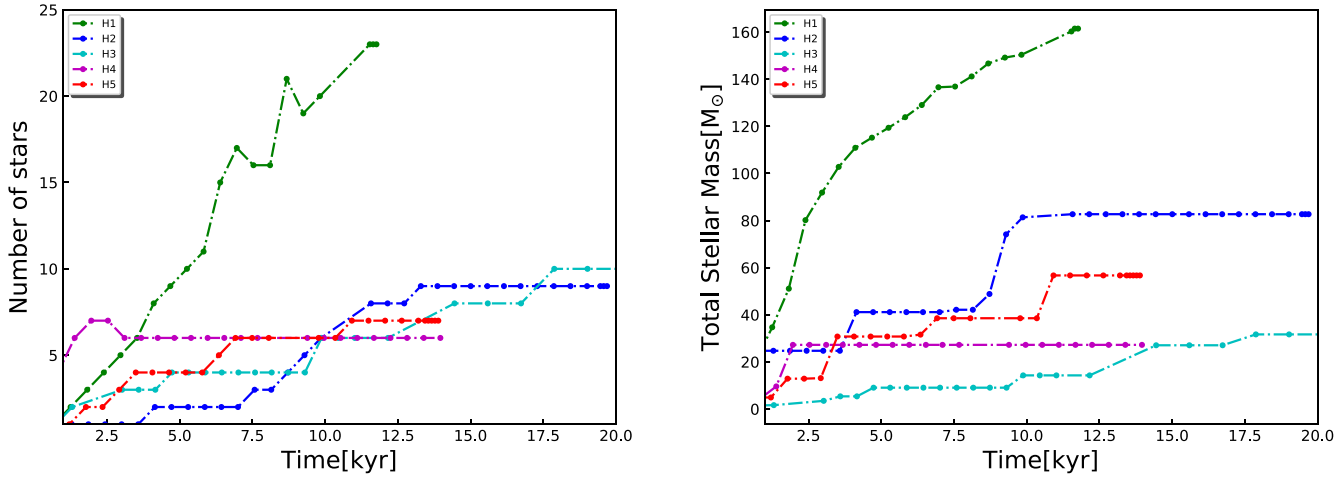

Figure 5. Time evolutions of the number of stars (left panel) and stellar masses (right panel) for all halos. Time is calculated after the formation of the first primary star in each halo.

fragments into multiple clumps, some of which later merge. The radiation from the massive stars and the dissipation heat from the merging of clumps suppress star formation for the last 10 kyr. A total of six stars form in halo 4 over 13 kyr.

The first star that forms in halo 5 is less than a solar mass, but it rapidly grows to 4.9 $M_\odot$ through accretion and a merger with another star that forms within its accretion radius. A second 8 $M_\odot$ star forms 1.3 kyr later. Two more 0.9 $M_\odot$ and 17 $M_\odot$ stars appear over the next kyr, and ionizing UV from the more massive star plows up a ring-like structure that later fragments into multiple clumps. After about 2.2 kyr, three more stars with masses of a few $M_\odot$ form over 4 kyr. A massive 18 $M_\odot$ star then forms, whose radiation blows away the surrounding gas and halts star formation for 34 kyr. A total of seven stars form in halo 5 over 14 kyr. The outflows driven by the stars expand to a few thousand astronomical units and collide with the dense infalling gas, which dissipates their energy.

We show the numbers of stars forming in the halos in the left panel of Figure 5. In general, they increase over time, except in halo 4. The total number of stars in halo 1 is 23: three are $> 20\ M_\odot$, five are $> 10\ M_\odot$, 11 are 1–10 $M_\odot$, and the rest are less than 1 $M_\odot$. The dips in the number of stars are due to the mergers with other stars. Nine stars form in halo 2 over 20 kyr: two have masses above 20 $M_\odot$, one is 16 $M_\odot$, three are 1–10 $M_\odot$, and three are less than 1 $M_\odot$. Ten stars form in halo 3 in 20 kyr: nine are 0.1–7 $M_\odot$ and one is 13 $M_\odot$. Only six stars form in halo 4 over 14 kyr: three are 1–5 $M_\odot$, one is 18 $M_\odot$, and two are $< 1\ M_\odot$. In halo 5, seven stars form over 14 kyr: two are above 10 $M_\odot$ (18 $M_\odot$ and 17 $M_\odot$), three are 4–8 $M_\odot$, and two are $< 1\ M_\odot$.

As shown in the right panel of Figure 5, the total stellar masses in the halos rise over time. The bumps in the plots correspond to the formation of massive stars at later times, and the plateaus are due to quiescent phases with no star formation. The final total stellar masses in halos 1–5 are 166, 83, 32, 27, and 57 $M_\odot$, respectively. Halo 1 has twice the average spin parameter of the minihalos, and the higher angular momentum of the disk results in more fragmentation, as found in previous studies (Latif et al. 2020; Patrick et al. 2020). Halo 2 has half the average minihalo spin parameter, and average accretion rates that are a factor of two smaller than those in halo 1.

Higher disk rotation rates and lower accretion rates produce less massive stars in halo 3, below 10 $M_\odot$. Only six stars form in halo 4, and only one is above 15 $M_\odot$. Lower accretion rates, rapid disk rotation, collisional dissociation of H_2 from mergers between clumps, and radiative feedback from stars produce the small number of stars in halo 4. Halos 4 and 5 have similar numbers of stars, but the total stellar mass of halo 5 is higher because two of its stars are greater than 15 $M_\odot$. The two halos were only evolved to 14 kyr, so more stars may form at later times and the total stellar mass may increase. All in all, the differences in the total stellar masses are due to the complex interplay between halo spin, the inflow rates onto the disks, and the radiative feedback from massive stars.

We show the mass distribution of the stars in our ensemble of halos in Figure 6. The stellar masses range from 0.1–40 $M_\odot$. Of the 55 stars, five are $> 20\ M_\odot$, seven are 10–20 $M_\odot$, 25 have masses of 1–10 $M_\odot$, and 18 are less than 1 $M_\odot$. About 69% of the total stellar mass is in the most massive stars ($\geqslant 10\ M_\odot$), suggesting a top-heavy IMF with $dN/dM \propto M_*^{-1.2}$. This IMF is consistent with previous studies (Susa et al. 2014; Stacy et al. 2016). Our results indicate that about 70% of the stars are ejected from their disks a few hundred yr after birth. Initially, radiation from the primary stars dislocates the centers of the disks, and three-body interactions with other stars later lead to their ejection. The majority of the ejected stars have masses below 10 $M_\odot$. The ejection velocities of these stars are a few kilometers per second, comparable to and in some cases even larger than the escape velocities of their host halos. This suggests that up to about ∼70% of Population III stars might be ejected from their host minihalos.

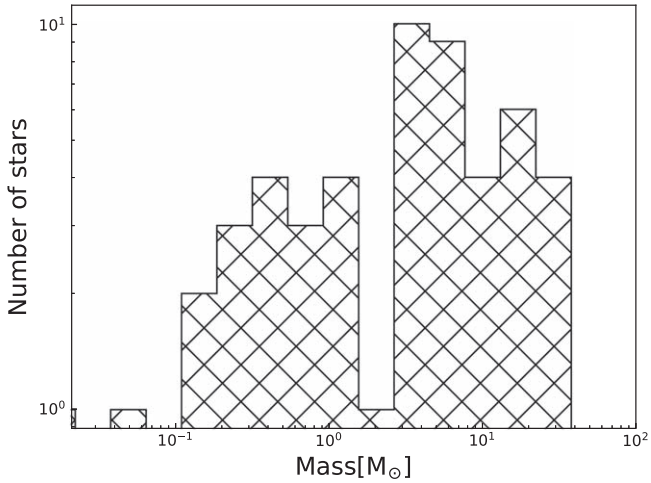

Figure 6. Distribution of the Population III star masses in the five halos.

The radial velocities and the ratio of the radial to the escape velocities for all of the stars are shown in Figure 7. They have typical radial velocities of a few kilometers per second, and most low-mass stars ($<5\ M_\odot$) have $v_{\rm rad}/v_{\rm esc}$ greater than 1. The low-mass stars are accelerated by dynamical interactions to velocities greater than $v_{\rm esc}$ and then ejected. Our results are in agreement with those of Greif et al. (2011, hereafter G11), who also find that low-mass protostars are ejected from the centers of clouds by dynamical interactions. Most of the stars in our models are located a few thousand au from the centers of the disks, while in G11 they are a hundred au from the center. This difference is due to the ionizing radiation in our simulations, which clears gas from the vicinity of the disk, and because our simulations are evolved 20 times longer than those in G11. Both factors contribute to the migration of the stars to larger radii. Given these differences, our results are qualitatively similar to those of G11.

Current numerical schemes treat stars as point masses, and cannot capture collisions between physically extended protostars. G11 approximated such collisions by relaxing the merging criteria of gravitational boundedness and allowing stellar mergers when they pass within 100 solar radii of each other, which led to more mergers in their simulations (so-called adhesive sink particles). Although we do not model the effect of gas-dynamical friction during stellar encounters, the accretion radius that we use is larger than that in G11, and helps to capture such mergers. Nevertheless, the inclusion of such friction could result in more mergers and fewer ejections.

4. Conclusion

Our models suggest that ionizing UV from massive stars and ejections due to three-body interactions impose characteristic masses of 1–10 $M_\odot$ on Population III stars. Stars that are

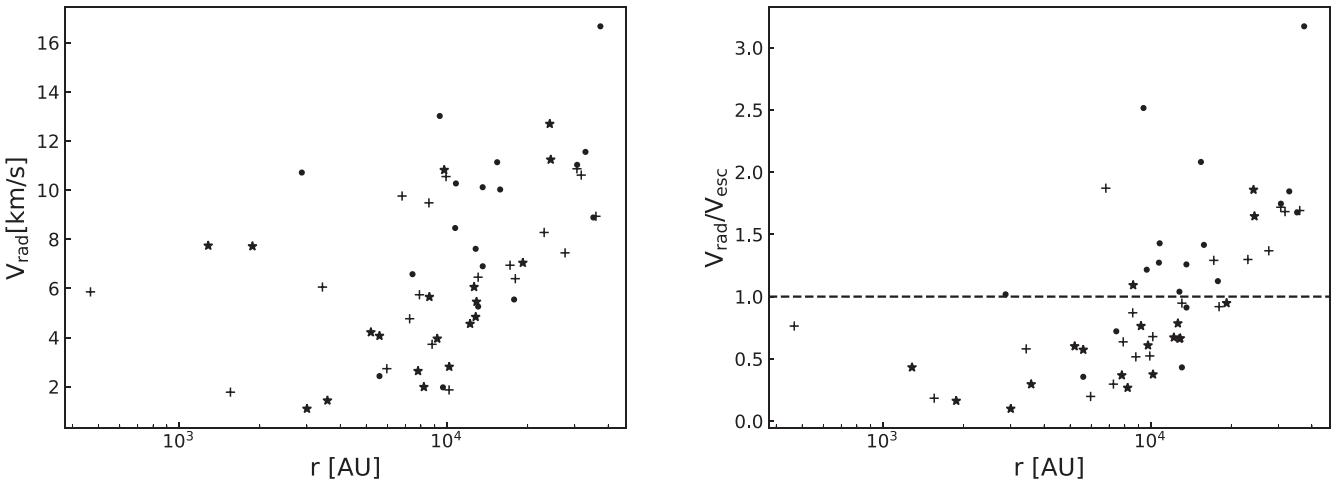

Figure 7. Radial velocities (left) and the ratio of radial velocity to escape velocity for all of the stars (right panel) as a function of their distance from the center of mass. The black dots, crosses, and stars denote stars with masses below 1 $M_{\odot}$, $1 < M_{*} < 5\ M_{\odot}$, and above 5 $M_{\odot}$, respectively. The escape velocity is calculated from the total enclosed mass interior to the current radial distance of the star from the center of mass.

ejected from their protostellar disks are cut off from the accretion flows that form them, and the ionizing UV from the most massive stars in the disk limits accretion onto the others. Up to 70% of Population III stars are ejected from their disks in our simulations, usually by a few hundred years after birth. Most of the ejected stars have masses below 10 $M_{\odot}$ and velocities of a few kilometers per second, comparable to and in a few cases greater than the escape velocities from their host halos. The characteristic Population III star masses in our simulation campaign are somewhat lower than those of previous studies, because those studies did not include ionizing UV feedback from all of the massive stars in the disk (and thus underestimated the effects of radiative feedback), and did not evolve the disks for long enough times in order to tally the ejections that terminated the growth of the stars.

We could not evolve the disks for longer than 20 kyr at resolutions of ∼10 au because the computational costs would have been prohibitive. Consequently, more stars may form at later times, and some may even reach higher masses, but we expect the overall shape of the IMF to remain the same. We also could not fully resolve the small-scale disks that may have formed around individual stars, possibly promoting accretion, and grow them to higher masses before the photoevaporation of the disk terminates their growth or they are ejected by three-body interactions. Fragmentation may also occur on smaller scales that are not resolved here. However, previous studies found that the clumps forming on such scales in protostellar disks are expected to migrate inward on short timescales and merge with the central star (Latif & Schleicher 2015; Hosokawa et al. 2016).

Our models do not capture all aspects of the premain-sequence evolution of Population III stars, but this does not strongly affect the dynamics of their outflows or the growth of the stars themselves. I-front radii mostly depend on ionizing photon emission rates, which we properly scale to stellar mass in our runs, and the expansion rate of the ionized flows depends on their temperatures, which are a weak function of the surface temperatures of the stars. We therefore expect that our approximate treatment of the protostars will properly capture their early growth. Our simulations neglect magnetic fields, which are thought to form even in primordial protostellar disks at high redshifts via amplification by turbulent dynamos on small scales (Schober et al. 2012; Turk et al. 2012; Latif & Schleicher 2016; Sharda et al. 2020). Magnetic field lines in the disk may stabilize the disk against fragmentation and produce fewer, more massive stars.

M.A.L. thanks the United Arab Emirates University for funding via the University Program for Advanced Research grant No. 31S390.

ORCID iDs

Muhammad A. Latif https://orcid.org/0000-0003-2480-0988
Daniel Whalen https://orcid.org/0000-0001-6646-2337
Sadegh Khochfar https://orcid.org/0000-0001-5956-7843

References

Abel, T., Anninos, P., Zhang, Y., & Norman, M. L. 1997, NewA, 2, 181
Abel, T., Bryan, G. L., & Norman, M. L. 2002, Sci, 295, 93
Anninos, P., Zhang, Y., Abel, T., & Norman, M. L. 1997, NewA, 2, 209
Bovino, S., Latif, M. A., Grassi, T., & Schleicher, D. R. G. 2014, MNRAS, 441, 2181
Bromm, V., Coppi, P. S., & Larson, R. B. 2002, ApJ, 564, 23
Bryan, G. L., Norman, M. L., O'Shea, B. W., et al. 2014, ApJS, 211, 19
Bullock, J. S., Dekel, A., Kolatt, T. S., et al. 2001, ApJ, 555, 240
Clark, P. C., Glover, S. C. O., Smith, R. J., et al. 2011, Sci, 331, 1040
Federrath, C., Banerjee, R., Clark, P. C., & Klessen, R. S. 2010, ApJ, 713, 269
Glover, S. C. O., & Abel, T. 2008, MNRAS, 388, 1627
Greif, T. H., Bromm, V., Clark, P. C., et al. 2012, MNRAS, 424, 399
Greif, T. H., Johnson, J. L., Klessen, R. S., & Bromm, V. 2008, MNRAS, 387, 1021
Greif, T. H., Springel, V., White, S. D. M., et al. 2011, ApJ, 737, 75
Hahn, O., & Abel, T. 2011, MNRAS, 415, 2101
Hirano, S., Hosokawa, T., Yoshida, N., et al. 2014, ApJ, 781, 60
Hirano, S., Hosokawa, T., Yoshida, N., Omukai, K., & Yorke, H. W. 2015, MNRAS, 448, 568
Hosokawa, T., Hirano, S., Kuiper, R., et al. 2016, ApJ, 824, 119
Hosokawa, T., Yorke, H. W., Inayoshi, K., Omukai, K., & Yoshida, N. 2013, ApJ, 778, 178
Hosokawa, T., Yorke, H. W., & Omukai, K. 2010, ApJ, 721, 478
Krumholz, M. R., McKee, C. F., & Klein, R. I. 2004, ApJ, 611, 399
Latif, M. A., Khochfar, S., Schleicher, D., & Whalen, D. J. 2021, MNRAS, 508, 1756
Latif, M. A., Khochfar, S., & Whalen, D. 2020, ApJL, 892, L4
Latif, M. A., & Schleicher, D. R. G. 2015, MNRAS, 449, 77
Latif, M. A., & Schleicher, D. R. G. 2016, A&A, 585, A151
Latif, M. A., Schleicher, D. R. G., Schmidt, W., & Niemeyer, J. 2013, ApJL, 772, L3

McGreer, I. D., & Bryan, G. L. 2008, ApJ, 685, 8
Omukai, K., & Palla, F. 2003, ApJ, 589, 677
Patrick, S. J., Whalen, D. J., Elford, J. S., & Latif, M. A. 2020, arXiv:2012.11612
Planck Collaboration, Ade, P. A. R., Aghanim, N., et al. 2016, A&A, 594, A13
Regan, J. A., & Downes, T. P. 2018, MNRAS, 478, 5037
Ripamonti, E., & Abel, T. 2004, MNRAS, 348, 1019
Schaerer, D. 2002, A&A, 382, 28
Schober, J., Schleicher, D., Federrath, C., et al. 2012, ApJ, 754, 99
Sharda, P., Federrath, C., & Krumholz, M. R. 2020, MNRAS, 497, 336
Smith, R. J., Hosokawa, T., Omukai, K., Glover, S. C. O., & Klessen, R. S. 2012, MNRAS, 424, 457
Stacy, A., Bromm, V., & Lee, A. T. 2016, MNRAS, 462, 1307
Sugimura, K., Matsumoto, T., Hosokawa, T., Hirano, S., & Omukai, K. 2020, ApJL, 892, L14
Susa, H. 2019, ApJ, 877, 99
Susa, H., Hasegawa, K., & Tominaga, N. 2014, ApJ, 792, 32
Turk, M. J., Oishi, J. S., Abel, T., & Bryan, G. L. 2012, ApJ, 745, 154
Whalen, D., & Norman, M. L. 2008, ApJ, 673, 664
Wise, J. H., & Abel, T. 2011, MNRAS, 414, 3458
Wise, J. H., Abel, T., Turk, M. J., Norman, M. L., & Smith, B. D. 2012, MNRAS, 427, 311
Wolcott-Green, J., Haiman, Z., & Bryan, G. L. 2011, MNRAS, 418, 838
Yoshida, N., Omukai, K., & Hernquist, L. 2008, Sci, 321, 669